The 60° dislocation in diamond and its dissociation

A T Blumenau[1,2]**, R Jones**[2] **and T Frauenheim**[1]

[1] Department of Physics, Universität Paderborn, D-33098 Paderborn, Germany
[2] School of Physics, University of Exeter, Exeter EX4 4QL, UK

E-mail: blum@phys.upb.de

Abstract
The perfect 60° glide dislocation in diamond serves as an example of how different aspects of dislocations can be modelled in an approach combining continuum elasticity theory with atomistic density-functional-based tight-binding calculations. After investigating the perfect 60° dislocation and its isolated Shockley partials, the energetics of dissociation are discussed. The 60° dislocation is found to dissociate with a substantial lowering of its line energy. However, an energy barrier to dissociation is found. The glide motion of the 30° Shockley partial involved is modelled in a process involving the thermal formation and subsequent migration of kinks along the dislocation line.

(Some figures in this article are in colour only in the electronic version)

1. Introduction

Diamond exhibits some interesting physical properties, like extreme hardness, high heat conductivity, high refractive index and a wide indirect electronic bandgap (5.49 eV) [1], which make it an interesting material not only as a gemstone but also for technological applications. Chemical vapour deposition (CVD) growth of diamond produces thin films, which might be used for semiconductor devices [2]. CVD-grown polycrystalline diamond reveals high densities of dislocations—sometimes up to 10^{12} cm^{-2} [3, 4], but also natural type IIa and IIb diamond contains up to 10^7 cm^{-2} [5–7]. Using weak-beam electron microscopy, Pirouz *et al* [8] found that dislocations in type IIa diamond are dissociated into glide partials separated by an intrinsic stacking fault (ISF) ribbon of width 25–42 Å. For the perfect 60° glide dislocation the dissociation reaction in the {111} plane into 30° and 90° Shockley partials is given as

$$\tfrac{1}{2}[1\bar{1}0] \longrightarrow \tfrac{1}{6}[1\bar{2}1] + \tfrac{1}{6}[2\bar{1}\bar{1}]. \tag{1}$$

This paper investigates only the perfect 60° glide dislocation and its partials. The dissociation reaction is discussed energetically and the dislocation glide of the 30° Shockley partial is modelled in a mechanism of kink formation and migration. As the 30° partial reconstructs in a double-period structure, the kink formation and dislocation glide processes are more complicated than those of the 90° single-period structure, which have been discussed earlier [9].
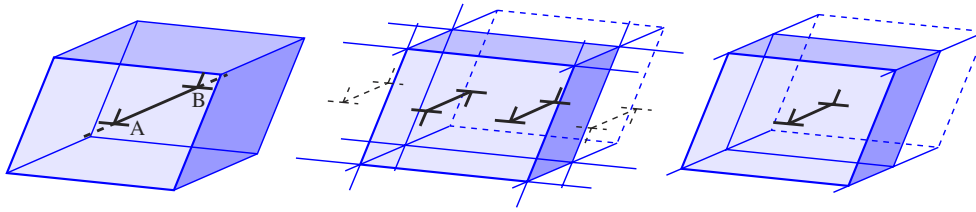
Figure 1. Schematic sketches of distinct atomistic dislocation models. Left: a cluster containing a single dislocation. A and B denote the points of dislocation–surface intersection. Middle: a dislocation dipole in a periodic supercell. Right: a dislocation in a supercell–cluster hybrid model, periodic along the dislocation line and cluster-like perpendicular to the line.

2. The modelling approach

2.1. Atomistic modelling

Two common atomistic approaches to describe dislocations in semiconductors are the *cluster* model and the *supercell* model.

In the cluster model a single dislocation is inserted into an atomic cluster representing the surrounding bulk crystal (see figure 1 (left)). In DFT-based methods where the electronic energy is explicitly included, the cluster surfaces are usually terminated with hydrogen atoms to avoid electronic gap states associated with dangling bonds or surface reconstructions, which might induce additional strain in the cluster core. However, the dislocation itself intersects with the cluster surface, which leads to an artificial distortion of the core structure close to the points of intersection. Hence the cluster has to be considerably extended in the direction of the dislocation line.

The periodic boundary conditions of the supercell model require an overall Burgers vector of $\vec{b}_{tot} = 0$. Therefore, the most simple configuration is that of a dipole with two dislocations of opposite Burgers vector included in a supercell. The situation is shown in figure 1 (middle), where the periodically repeated images of the dislocation are indicated in one dimension as an example. The main disadvantage of the pure supercell model stems from the elastic dislocation–dislocation interaction within and across the cell boundaries to neighbouring cells. This effect can be considerable as in the case of a dipole, for example, the two dislocations are separated by a distance of only half the cell period length in the respective direction. Even though the elastic interaction can be described analytically and can be subtracted from the calculated energy [10, 11], the core structure and reconstruction still depends on the stress state. Therefore the stress of the selected supercell geometry influences the core structure and possibly the core energy.

To avoid the problems arising from pure cluster and supercell models, in this work we combine both into a *supercell–cluster hybrid* approach: the dislocation is placed in a model which is periodic along the dislocation line. However, it is non-periodic perpendicular to the line direction with a hydrogen-terminated surface [12, 13] (see figure 1 (right)). This approach respects the dislocation periodicity along the line direction, avoiding surface intersections, and at the same time the model only contains a single isolated dislocation, avoiding dislocation–dislocation interactions. This makes the hybrid model well adapted to line defects. In section 3 size convergence of the hybrid model will be tested in comparison with linear elasticity theory.

2.2. Computational

For the atomistic modelling we use a density-functional-based tight-binding (DFTB) approach. In this approach the electronic wavefunctions are approximated by a linear combination of

atomic orbitals (LCAO) involving a minimal basis set of s and p valence orbitals. The two-centre Hamiltonian and overlap matrix elements result from atom-centred valence electron orbitals and the atomic potentials from single-atom calculations in density-functional theory (DFT). Exchange and correlation contributions in the total energy as well as the ionic core–core repulsion are taken into account via a repulsive pair potential. The latter is obtained by comparison with DFT calculations. Thus the DFTB method can be seen as an approximate density-functional scheme [14, 15]. In this approach all DFT integrals (Hamiltonian and overlap matrix) as well as the repulsive potential can be calculated in advance and are tabulated over the interatomic distance of two atoms. This considerably reduces the computational effort, allowing the treatment of larger models compared to less approximate DFT-based methods.

In this work all structures are geometrically optimized using a conjugate gradient algorithm until all forces are well below 5×10^{-3} eV Å^{-1}.

3. The perfect 60° dislocation and its Shockley partials

3.1. Core structures

Atomistic models of dislocations can be constructed by displacing the atoms of an appropriate supercell–cluster hybrid according to their Burgers vector $\vec{b}$ and their line direction $\vec{\ell}$. If required, an additional half-plane of atoms or an ISF has to be introduced. The dislocation core structures so obtained, however, are nothing more than a mere first guess and hence have to be structurally optimized. As mentioned in section 2.2, in this work this is achieved by a conjugate gradient algorithm. The chosen models have a period twice that of the cubic lattice, $a_0 \langle 110 \rangle$, and have a radius $\sim 3.5a_0$, with a_0 being the lattice constant. Thus the unit cell contains ~ 600 atoms. The resulting low energy core structures are shown in figure 2. As the principal structures have been presented before [9, 16], they will only be discussed briefly here.

The perfect 60° glide dislocation is obtained by inserting (or removing) a {111} half-plane of atoms. Figure 2 shows the half-plane framed with lines. The relaxed core structure shows bond reconstruction of the terminating atoms of the half-plane with neighbouring atoms. Reconstruction bonds along the dislocation line impose a double-period structure.

The 30° glide partial reconstructs forming a line of bonded atom pairs. The structure is double-periodic and the reconstruction bonds are 18% stretched compared to bulk diamond.

For the 90° glide partial there are two principal structures: a single-period (SP) and a double-period (DP) reconstruction. The SP structure results simply from forming bonds in the glide plane connecting the faulted region with the bulk region. These bonds are 13% stretched. The DP structure can be obtained from the SP structure by introducing alternating kinks. Here the deviation from the bulk bond length is slightly less. The DP structure was first proposed for silicon by Bennetto *et al* [17].

3.2. The elastic energy as a size convergence criterion

Whenever modelling defects in semiconductors on an atomistic level, one has to test whether the chosen model geometry is suitable and if its size, or in other words the number of atoms considered, is sufficient to describe the defect as embedded in an otherwise perfect crystal lattice. In particular for dislocations, which are extended structural defects of the lattice with a considerable strain field, a sufficient model size is crucial if the surface of the model is relaxed freely. This convergence in size can be checked in comparison with elasticity theory. As we
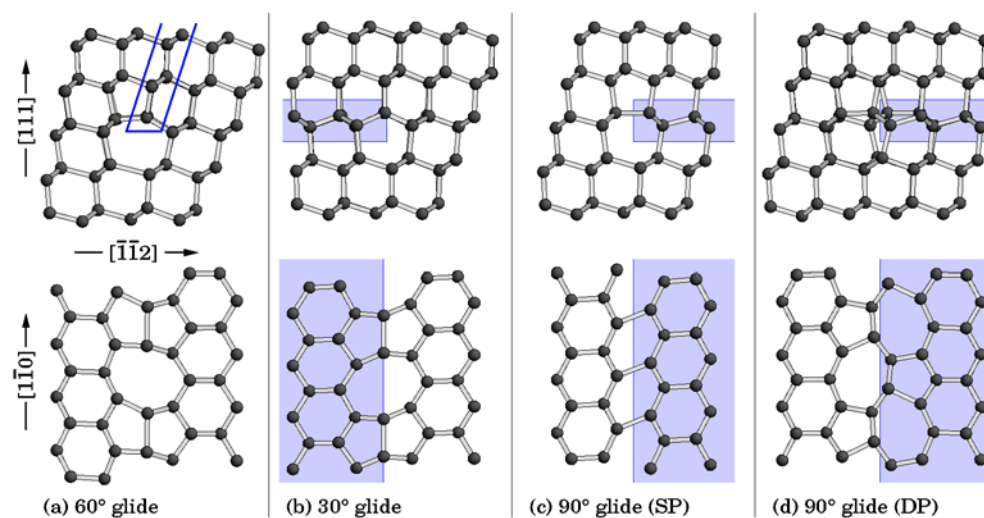
Figure 2. The relaxed core structures of (a) the undissociated 60° glide dislocation, (b) the 30° partial, (c) and (d) the 90° partial. In the latter case SP and DP denote the single-period and double-period core reconstruction. For each structure, the upper figure shows the view along the dislocation line projected into the $(1\bar{1}0)$ plane and the lower figure shows the (111) glide plane. The region of the ISF accompanying the partials is shaded in the respective structures.

know, the elastic energy $E(R)$ contained in a cylinder of radius R centred on the dislocation core shows logarithmic behaviour in the continuum limit. For each length L we obtain [18]

$$\frac{E(R)}{L} = \frac{k|\vec{b}|^2}{4\pi} \ln\left(\frac{R}{R_c}\right) + \frac{E_c}{L}, \qquad R \geqslant R_c. \tag{2}$$

Here R_c is the core radius and E_c is the corresponding core energy—both values are inaccessible by continuum elasticity theory. The energy factor k depends on the elastic constants and the angle between the Burgers vector and the line direction. To compare now the spatial distribution of the formation energy in a dislocated supercell–cluster hybrid with the elastic energy, as given in equation (2), one has to sum over the atom projected energy of all atoms in a cylinder of radius R and length L following the corresponding geometry. If the model contains a stacking fault, the energy of the fault has to be subtracted. This procedure then yields the radial formation energy, $E_f(R)/L$, per unit length.

Figure 3 shows $E_f(R)/L$ for 30° partial hybrid models of three different sizes (A 182, B 462 and C 870 carbon atoms) plotted against $\ln(R)$. All three graphs show approximately linear behaviour from a core radius $R_c = 3.1$ Å onwards. The corresponding core energy is $E_c/L = 0.88$ eV Å^{-1}. Of course the core radius is only vaguely defined and it is somewhat arbitrary what one calls 'approximately linear'. The gradient of the linear part should be given as the pre-logarithmic factor in equation (2). Anisotropic elasticity theory, as described in [19] and [18], yields $k(\beta) = 553$ GPa using the DFTB elastic constants ($c_{11} = 1116$ GPa, $c_{12} = 172$ GPa, $c_{44} = 606$ GPa). The corresponding gradient is drawn in figure 3 and the correspondence seems to be reasonably good. The oscillations in all curves are an effect of the discrete sum and they should disappear in the limit $R \to \infty$. From a certain radius onwards, the energy in each of the graphs increases rather rapidly and non-linearly. This can be explained by the radius getting too close to the surface of the respective model, where the strained bulk lattice is not represented sufficiently since surface effects dominate. For even larger radii the integration cylinder is not completely contained in the model and strain contributions from the
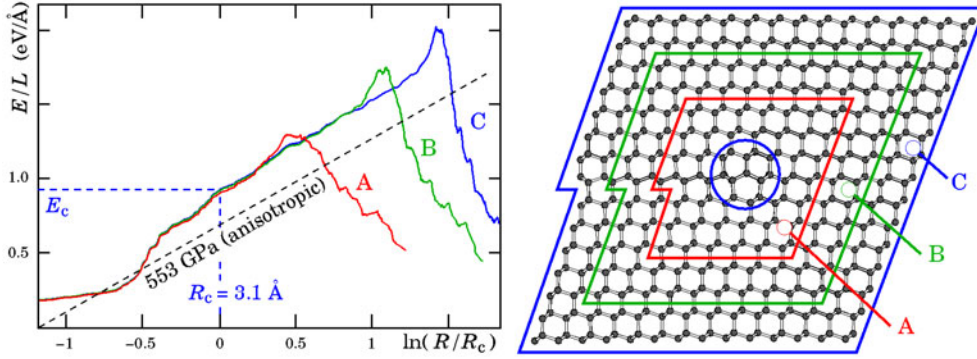
Figure 3. The radial formation energy $E_f(R)/L$ of the 30° glide partial for hybrid models of different sizes. Left: $E_f(R)/L$ for hybrid model A (182 carbon atoms), B (462 carbon atoms) and C (870 carbon atoms). The gradient of the broken line corresponds to the elastic energy in equation (2) with $k = 553$ GPa, a result obtained in *anisotropic* elasticity theory. The core radius R_c and energy E_c can be obtained directly from the graph. See the text for a detailed description. Right: a section through the three corresponding hybrid models (($1\bar{1}0$) plane). The hydrogen termination at the surface is not shown. The inner white area marks the core region ($R_c = 3.1$ Å). The subsequently surrounding areas give the dimensions of the three respective models.

Table 1. Core radii R_c and core energies E_c. To facilitate comparison between different dislocations with different core radii, the core energy E_c' corresponding to a radius of 6 Å is introduced.

	60°	30°	90° (SP)	90° (DP)
R_c (Å)	4.1	3.1	3.0	3.3
E_c/L (eV Å^{-1})	2.13	0.88	1.32	1.18
$E_c'(R = 6$ Å$)/L$ (eV Å^{-1})	2.55	1.23	1.74	1.57

model's edges lead to a sudden breakdown of the formation energy. Hence one can directly conclude from figure 3 that the maximum radius where the models give a good representation of the surrounding strained bulk lattice—at least in terms of elasticity—is about 4.2, 8.4 and 12.4 Å for models A, B and C, respectively. In other words, in principle the smallest model with 182 carbon atoms is able to describe the dislocation as embedded in an otherwise perfect crystal. However, to be on the safe side for dislocations with larger R_c, in this work supercell–cluster hybrid models similar in size to B are used.

Table 1 gives the core radii and energies for all dislocations discussed in this work. A direct comparison of core energies only makes sense between dislocations of the same angle β between Burgers vector and line direction. Further, since the core radius R_c usually varies with different dislocations, one should not compare $E_c = E(R_c)$ but $E_c' = E(R')$ for an arbitrary radius $R' \geqslant R_c$ common to all dislocations. Here the choice is $R' = 6$ Å. Comparing the relative stability of the DP and the SP structures of the 90° partial, low-stress quadrupole calculations of Blase *et al* [11] yield 169–198 meV Å^{-1}—in good agreement with the $\sim$170 meV Å^{-1} difference found in this work.

As mentioned earlier, the determination of the core radii is somewhat arbitrary. Hence one should not draw strong conclusions from R_c. However, the core radius seems to depend on the Burgers vector: the undissociated 60° dislocation, which has the largest Burgers vector, appears with the largest core radius.
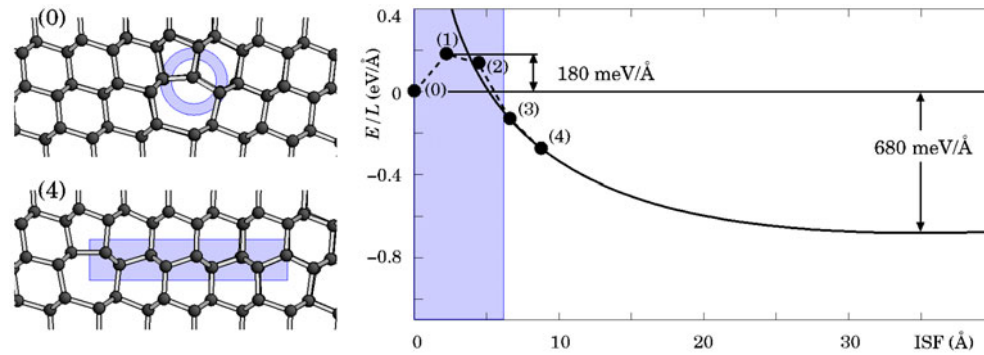
Figure 4. Structure and energetics of the dissociation of the 60° dislocation into a 90° and 30° partial. Left: the view is projected into the $(1\bar{1}0)$ plane. The top structure labelled (0) shows the undissociated perfect dislocation. The stacking fault in the fourth (4) dissociation step is shaded. Right: the dissociation energy. The relative atomistic DFTB energies of the first four dissociation steps and of the undissociated dislocation are labelled (1)–(4) and (0), respectively. Zero energy is set to the undissociated dislocations. The full lines represent the sum of the stacking fault energy and the elastic interaction energy as given in continuum elasticity theory [18]. Shading below ∼6 Å indicates the region where the two core radii of the respective partial dislocations overlap—the region where continuum elasticity theory fails.

4. Dissociation of the perfect 60° dislocation

When it comes to the dissociation of perfect dislocations into Shockley partials, then the two competing energy contributions in the elastic limit are the stacking fault energy and the elastic partial–partial interaction energy. The first grows proportionally with the partial–partial separation R and the interaction energy lessens logarithmically [18]. Unfortunately the energy offset of the elastic interaction is unknown and consequently, by means of elasticity theory only, a complete energy balance is impossible. Only the equilibrium distance of dissociation can be predicted—34 Å using experimental stacking fault energies and elastic constants, and 35 Å based on the respective values obtained with the DFTB method [16]. This agrees well with observed dissociation widths between 25 and 42 Å [8]. The large variation might be either due to the rather flat energy minimum at the equilibrium distance or pinning of dislocations by point defects preventing the equilibrium stacking fault width being attained.

To obtain the unknown energy offset in the elastic interaction, the dissociation process is modelled atomistically in a large supercell–cluster hybrid containing about 700 atoms. Without the core regions of the partials getting too close to the hybrid's surface, this size allows dissociation up to the fourth step (a stacking fault width of 8.75 Å). Figure 4 shows the relaxed geometries for the respective undissociated dislocation and the fourth step of dissociation into a 30° and a 90° (SP) partial as well as the corresponding discrete relative energies. Since the 90° (DP) has a similar core bonding configuration, a similar result would be expected. Now the sum of the ISF energy and the elastic interaction energy has to be adjusted to the atomistic DFTB energy of the fourth dissociation step. In other words, the atomistic calculation is extrapolated towards arbitrary dissociation distances by means of elasticity theory. In figure 4 the resulting continuous energies are drawn as full lines for both dislocation types. One can observe that the atomistic calculation and continuum theory still agree for the third stage of dissociation. For smaller stacking fault widths in the region of overlapping dislocation core radii, however, the deviation becomes obvious and finally for $R \to 0$ the continuum result diverges.
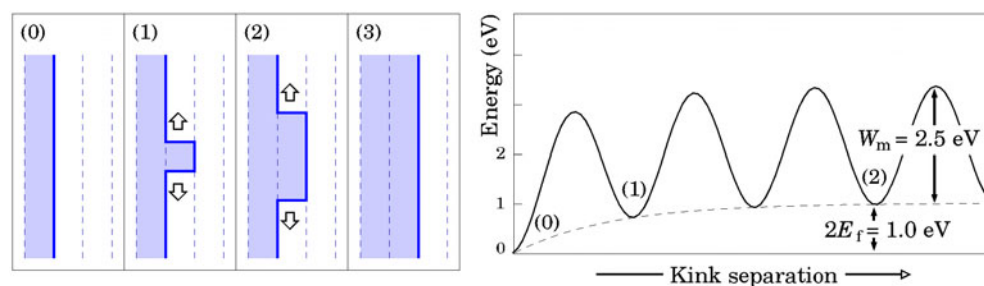
Figure 5. Kink formation and migration at the 90° partial dislocation. Left: dislocation glide of partials by kink formation and migration. The Peierls valleys are drawn as broken lines. (0) shows the straight dislocation line in one valley, while in (1) a kink pair has formed, whose single kinks then migrate along the dislocation line (2). Finally, in (3), the shown segment of the dislocation has moved to the next Peierls valley. Right: schematic representation of the energy of the glide process. The broken line connecting the minima represents the formation energy of the kink pair. The energy contribution of the expanding stacking fault is not included in the graph.

An interesting feature is the presence of an energy barrier of $\sim$180 meV Å^{-1} to initiate dissociation of the 60° dislocation. This barrier should have a considerable effect, since it is approximately 5 Å wide and cannot be overcome in a single step. This might explain the presence of undissociated 60° dislocations, as observed in weak-beam electron microscopy [8] and recently in high resolution electron microscopy [20].

5. Kinked dislocations and glide motion

Dislocation glide arises from an external stress acting on the dislocation leading to the creation of kinks. When the stress is insufficient to overcome the Peierls barrier, kinks must be generated by a thermal process and motion occurs by their migration along the dislocation line (see figure 5 (left)). In the case when obstacles (point defects and impurities) are not present, and for short dislocation segments, the velocity is controlled by the double kink formation energy $2E_f$ and the kink migration barrier W_m [18]: $Q = 2E_f + W_m$ gives the activation energy. $2E_f$ can be obtained by comparing atom clusters of the same shape and stoichiometry, where one contains a straight dislocation segment, and one a double kinked segment. The elastic kink–kink interaction energy has to be subtracted. As one kink migration step involves only two atoms which move considerably, it can be parametrized by their movement and W_m can be obtained at the saddle point. For the 90° (SP) this procedure yields $2E_f = 1.0$ eV and $W_m = 2.5$ eV, as demonstrated in [9] and illustrated in figure 5 (right).

In this work, the main emphasis lies on the glide process of the 30° partial—a DP structure. Here the situation is much more diverse than at the 90° (SP), where only one principal kink structure occurred: depending on the kink position relative to the 30° partial reconstruction bonds, two different structures for the left kink as well as for the right kink are possible. In figure 6 (upper and middle panels) these different structures are labelled LK1, LK2 and RK1 and RK2 for the two left and right kinks, respectively.

To determine the kink formation energies, clusters similar to those for the 90° partial in [9] are used. However, unlike the 90° partial, the structures of left and right kinks are very different, and therefore a similar formation energy cannot be expected. Since in a cluster the formation energy of a single kink cannot be determined, it is only possible to obtain the sum of the formation energies of two different kinks. The elastic kink–kink interaction energy
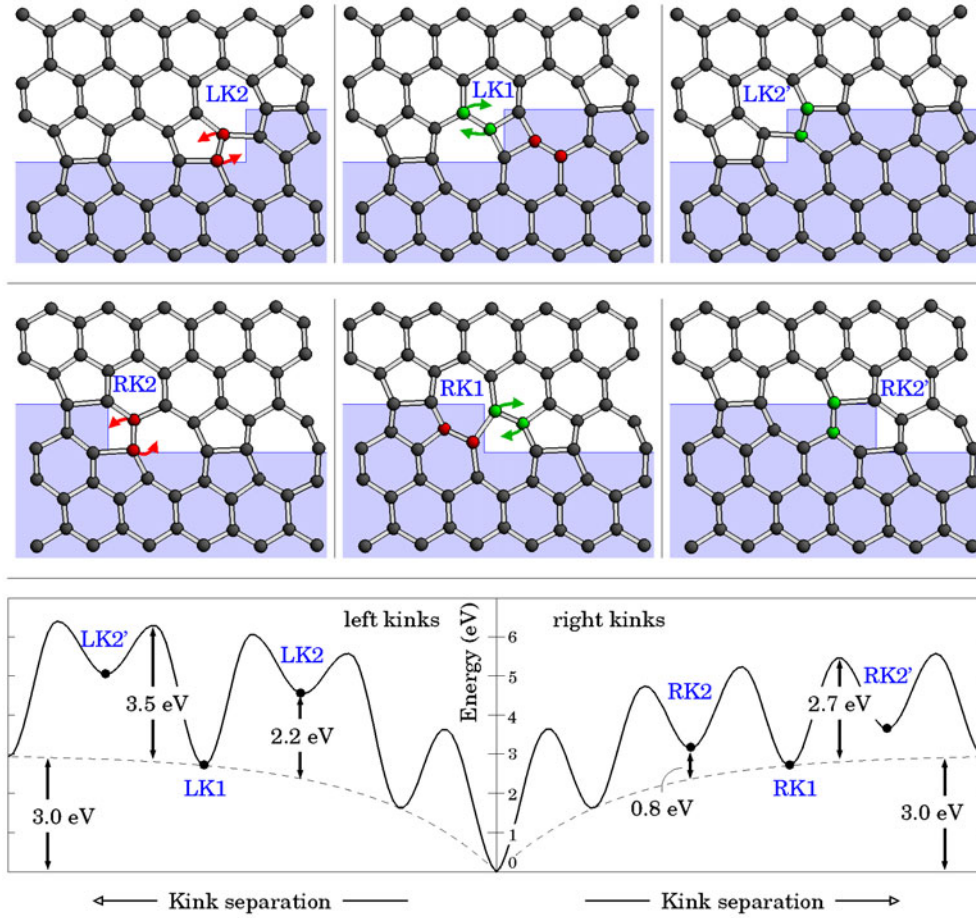
Figure 6. Kink formation and migration at the 30° partial dislocation. Upper panel: the elementary kink migration steps of the left kink LK2 → LK1 → LK2′. The relaxed structures of a starting kink LK2, and the subsequent kinks LK1 and LK2′, are shown projected into the glide plane. The faulted region is shaded and arrows indicate the motion of the two atoms involved. Middle panel: the elementary kink migration steps of the right kink RK2 → RK1 → RK2′. Lower panel: schematic representation of the energy of the glide process. Since for the 30° partial the migration barriers differ for left and right kinks, the corresponding processes are shown separately. The broken curve connecting the minima represents the formation energy of the low energy kink pair. The energy contribution of the expanding stacking fault is not included in the graph.

$E_{\mathrm{LK,RK}}(L)$ has to be subtracted [18]:

$$E_{\mathrm{LK,RK}}(L) = -\frac{\mu\,a^2}{32\pi L}\,\frac{4+\nu}{1-\nu}\,|\vec{b}_{30}|^2. \tag{3}$$

Here L is the kink–kink distance, a is the kink height and μ and ν are the shear modulus and Poisson's ratio, respectively. We obtain by comparison between different pairing of kinks in a double kink:

$$E_{\mathrm{f}}(\mathrm{LK1}) + E_{\mathrm{f}}(\mathrm{RK1}) = 3.0 \text{ eV}$$
$$E_{\mathrm{f}}(\mathrm{LK2}) = E_{\mathrm{f}}(\mathrm{LK1}) + 2.2 \text{ eV}$$
$$E_{\mathrm{f}}(\mathrm{RK2}) = E_{\mathrm{f}}(\mathrm{RK1}) + 0.8 \text{ eV}.$$

LK1 and RK1 are the lowest energy kinks. Thus in the kink migration process it is an LK1–RK1 double kink that will be preferentially formed at the initial stage. However, subsequent migration inevitably involves the two high energy kinks as intermediate structures.

As shown in figure 6, the expansion of the double kink can be described as a succession of two-atom processes. To find the intermediate saddle point structure between two kink positions, the elementary kink migration step is parametrized by the coordinates of each of the two core (primary) atoms at the end of the kink projected onto the connecting line between their initial and final positions. The whole structure is structurally relaxed, subject to the constraint that the two primary atoms are constrained to lie in a plane perpendicular to the connecting line between their initial and final positions. Varying the two parameters independently yields a two-dimensional energy surface and thus the saddle point can be determined. The barriers for left and right kink migration indicate the right kink as the more mobile one:

$$W_{\mathrm{m}}(\mathrm{LK}) = 3.5 \text{ eV}$$
$$W_{\mathrm{m}}(\mathrm{RK}) = 2.7 \text{ eV}.$$

Figure 6 (lower panel) shows the resulting energy of the glide process at the 30° partial for a moving left and right kink separately. The velocity of the 30° partial depends on the energies and barriers as follows [21]:

$$v_{\mathrm{disl}} \propto \exp\left(-\frac{E_{\mathrm{f}}(\mathrm{LK1}) + E_{\mathrm{f}}(\mathrm{RK1})}{kT}\right)\left[\exp\left(-\frac{W_{\mathrm{m}}(\mathrm{LK})}{kT}\right) + \exp\left(-\frac{W_{\mathrm{m}}(\mathrm{RK})}{kT}\right)\right]. \tag{4}$$

With an average activation energy to glide motion around $Q_{30} \approx 6$ eV (short dislocation segments) the 30° partial appears to be far less mobile than the 90° partial ($Q_{90} = 3.5$ eV). Hence the latter can be expected to move faster under applied stress and raised temperatures. The stacking fault width will then increase if the mobile partial leads, increasing the back stress and hence slowing it down. The reverse happens if the mobile partial trails.

6. Summary and conclusions

In this work the 60° glide dislocation in diamond and its dissociation into Shockley partials has been investigated in atomistic supercell–cluster hybrid models. In this approach elasticity theory has proven invaluable to describe the long range elastic strain effects associated with dislocations and also served as a good convergence criterion for the size of the atomistic models used. The atomistic modelling (using the DFTB method) allowed a convenient determination of dislocation core energies and of the energy offset in the dissociation of dislocations. In elasticity theory the latter properties are both inaccessible.

A barrier of around 180 meV Å^{-1} to the dissociation of the perfect 60° dislocation into a 30° and a 90° Shockley partial was found. This barrier might explain the experimental observation of undissociated 60° dislocations, even though an overall energy gain of around 680 meV Å^{-1} strongly favours dissociation.

The glide motion of the 30° partials has been considered as a process of kink formation and subsequent migration and results were compared with those for the 90° partial. The latter proves to be the far more mobile species, with a thermal activation energy of 3.5 eV (the sum of the double-kink formation energy and the migration barrier) for short dislocation segments. At the 30° glide partial the migration barriers are, on average, 0.5 eV larger and the double-kink formation energy exceeds that of the 90° partial by 2 eV. The resulting average thermal activation energy of the 30° glide partial is found to be $Q_{30} \approx 6$ eV.

In diamond the lowest energy structure of the undissociated screw resembles two 30° partials in the same Peierls valley with a sp^2 hybridized core [22, 23]. Dissociation of this

structure results in two 30° partials of the same type as investigated in this work. Therefore the calculated glide activation energies apply to the dissociated screw dislocation as well.

References

[1] Lang A R 1982 *The Properties of Diamond* ed J E Field (New York: Academic) p 425
[2] Isberg J, Hammersberg J, Johansson E, Wikström T, Twitchen D J, Whitehead A J, Coe S E and Scarsbrook G A 2002 *Science* **297** 1670
[3] Graebner J E, Reiss M E, Seibles L, Hartnett T M, Miller R P and Robinson C J 1994 *Phys. Rev.* B **50** 3702
[4] Steeds J W, Mora A E, Butler J E and Bussmann K M 2002 *Phil. Mag.* A **82** 1741
[5] Kiflawi I and Lang A R 1974 *Phil. Mag.* **30** 219
[6] Hanley P L, Kiflawi I and Lang A R 1977 *Phil. Trans. R. Soc.* A **284** 330
[7] Sumida N and Lang A R 1981 *Phil. Mag.* A **43** 1277
[8] Pirouz P, Cockayne D J H, Sumida N, Hirsch P and Lang A R 1983 *Proc. R. Soc.* A **386** 241
[9] Blumenau A T, Fall C J, Jones R, Heggie M I, Briddon P R, Frauenheim T and Öberg S 2002 *J. Phys.: Condens. Matter* **14** 12741
[10] Arias T A and Joannopoulos J D 1994 *Phys. Rev. Lett.* **73** 680
[11] Blase X, Lin K, Canning A, Louie S G and Chrzan D C 2000 *Phys. Rev. Lett.* **84** 5780
[12] Blumenau A T, Elsner J, Jones R, Heggie M I, Öberg S, Frauenheim T and Briddon P R 2000 *J. Phys.: Condens. Matter* **12** 10223
[13] Northrup J E 2001 *Appl. Phys. Lett.* **78** 2288
[14] Porezag D, Frauenheim T, Köhler T, Seifert G and Kaschner R 1995 *Phys. Rev.* B **51** 12947
[15] Frauenheim T, Seifert G, Elstner M, Hajnal Z, Jungnickel G, Porezag D, Suhai S and Scholz R 2000 *Phys. Status Solidi* b **217** 41
[16] Blumenau A T, Heggie M I, Fall C J, Jones R and Frauenheim T 2002 *Phys. Rev.* B **65** 205205
[17] Bennetto J, Nunes R W and Vanderbilt D 1997 *Phys. Rev. Lett.* **79** 245
[18] Hirth J P and Lothe J 1982 *Theory of Dislocations* 2nd edn (New York: Wiley)
[19] Teutonico L J 1962 *Phys. Rev.* **127** 413
[20] Willems B 2002 private communication (EMAT, University of Antwerp)
[21] Nunes R W, Bennetto J and Vanderbilt D 1998 *Phys. Rev.* B **57** 10388
[22] Pizzagalli L, Beauchamp P and Rabier J 2002 *J. Phys.: Condens. Matter* **14** 12681
[23] Blumenau A T, Jones R, Frauenheim T, Willems B, Lebedev O I, Van Tendeloo G, Fisher D and Martineau P M 2003 *Phys. Rev.* B **68** 014115